PCCP

ROYAL SOCIETY OF CHEMISTRY

PAPER

View Article Online
View Journal | View Issue

Cite this: *Phys. Chem. Chem. Phys.*, 2024, **26**, 29466

Neutron imaging for automotive polymer electrolyte fuel cells during rapid cold starts†

Wataru Yoshimune, *[a] Yuki Higuchi, [a] Fangzhou Song,[b] Shogo Hibi,[a] Yoshihiro Matsumoto,[c] Hirotoshi Hayashida,[c] Hiroshi Nozaki,[a] Takenao Shinohara[b] and Satoru Kato[a]

Received 21st September 2024,
Accepted 15th November 2024

DOI: 10.1039/d4cp03646h

rsc.li/pccp

The phase transition from supercooled water to ice is closely related to the electrochemical performance and lifetime of an energy device at sub-zero temperatures. In particular, fuel cells for passenger cars face this issue because they are frequently started and stopped under sub-zero conditions during the winter season. However, there is a lack of visual information regarding the processes that occur within the fuel cell stack, and insight into how to improve the safety and performance during cold starts is lacking. In this study, we developed an *operando* neutron imaging system to visualise the water distribution inside an automotive single cell simulating a fuel cell stack during cold starts. This was achieved using a rapid heating unit. In addition, we showcased cold-start tests at three different sub-zero temperatures, and the obtained results suggest that pre-conditioning residual water and post-cold-start meltwater have an impact on the rapid cold-start performance.

Introduction

In cold climates, ice can form inside water-containing electrochemical energy devices, including polymer electrolyte fuel cells (PEFCs),[1,2] water electrolysers[3–5] and carbon dioxide reduction cells.[6,7] The adverse effects of freezing water inside the electrodes of these devices pose a risk of cold-start failure and material degradation.[8,9] This climate-related issue is particularly pronounced in PEFCs that are used in passenger-oriented fuel cell electric vehicles (FCEVs) with frequent start–stop cycles.[10]

The hydrated proton exchange membrane (PEM) present in PEFCs is known to retain proton conduction at temperatures as low as −40 °C, allowing for faradaic current transfer between the electrodes during cold starts. For a successful cold start at sub-zero temperatures, the cell must be warmed above 0 °C before the produced water freezes. In a commercial FCEV, the fuel cell stack is operated with the priority of generating sufficient waste heat to warm the stack quickly, while simultaneously providing electrical power to the vehicle during the cold start.[11]

Cold-start failure is caused by ice aggregation, which occurs due to freezing of the produced water, and interrupts the air supply to the cathode. The metastable supercooled water produced at the cathode suppresses freeze-out, thereby providing time for heat generation during cold starts.[12,13] The freezing mechanism and its adverse effects have long been debated in the contexts of material development[14,15] and protocol optimisation.[9,16–18] Indeed, many *operando* and *post-mortem* studies have shown that the cold-start temperature affects the location of ice aggregation at the cathode electrode, including the catalyst layer (CL), the gas diffusion layer (GDL), and the gas flow channels. Although ice formation has been observed at the cathode CL after a cold start from cryogenic conditions below −10 °C,[19–26] ice aggregates have also been visualised in the cathode gas flow channels during a cold start from mild conditions (−10 to −5 °C).[27–32] Failure due to ice blockage in the cathode GDL and gas flow channels can be identified by a high pressure drop from the cathode inlet to the outlet,[31,33] while a drop in the current density without a corresponding pressure drop implies ice formation in the cathode CL.[33]

In cold-start research, a gap exists between academic research and industrial development owing to the prohibitive cost of stack tests. The fact that the number of patents per year exceeds the number of journal articles further confirms this gap.[34] Cold-start studies usually involve two types of experimental protocols, namely non-isothermal and isothermal protocols. Previously, a non-isothermal protocol was used to investigate the ability of a stack to start by self-heating. This study was relevant for commercial applications, with such measurements typically aiming to confirm that the stack can reach temperatures above 0 °C before cold-start failure occurs due to the presence of frozen water.[17,18,35] In general, a fuel cell

[a] *Toyota Central R&D Labs., Inc., Nagakute 480-1192, Japan. E-mail: yoshimune@mosk.tytlabs.co.jp*
[b] *J-PARC Center, Japan Atomic Energy Agency, Tokai 319-1195, Japan*
[c] *Comprehensive Research Organization for Science and Society, Tokai 319-1106, Japan*

† Electronic supplementary information (ESI) available. See DOI: https://doi.org/10.1039/d4cp03646h

stack requires waste heat from multiple cells within a stack to overcome the heat capacity of the end plates during a cold start; therefore, a stack of more than 20 cells is typically required.[36] In contrast, academic research typically uses small single cells to understand the freezing mechanism during an isothermal cold start at moderate sub-zero temperatures.[12–15,19–26,28–32] Such isothermal tests examine the water storage capacity before cold-start failure by applying a minimal galvanostatic load for minimal water and heat production rates. The effects of heat transfer[36] and cell size[37] on the cold-start performance are often ignored or trivialised, and so efforts should be focused on bridging the gap between the findings of academic research and actual fuel cell stack development.

In recent years, our research group established a technique for visualising water inside PEFCs. This is based on the use of *operando* neutron imaging at the RADEN facility of the Japan Proton Accelerator Research Complex (J-PARC).[38] The water behaviour in a 2nd generation FCEV (MIRAI, Toyota Moter Corporation, Japan) was examined at 60 °C, and the inhomogeneous in-plane liquid water distribution induced by water back-diffusion from the cathode to anode was revealed.[39] In addition, our group also proposed a method for water/ice identification in a water/ice mixture using pulsed neutron beams[40,41] and demonstrated the water/ice distribution in a 2nd generation MIRAI at sub-zero temperatures.[42]

Thus, we herein report the establishment of a system to assess the water distribution in automotive single cells during a rapid cold start. For this purpose, a heat-assisted device was employed to reproduce the heat transfer and current behavior of a single cell within a fuel cell stack. The aim of this study is to showcase the in-plane water distribution in a 2nd generation MIRAI during cold starts at different sub-zero temperatures, in addition to revealing the thawing behavior during rapid cold starts.

Results

Operando neutron imaging system

An automotive PEFC used in a stack of a 2nd generation MIRAI[35,39,42–44] was placed in an environmental chamber purged with a dry air flow to maintain the dew point below −30 °C. The *operando* neutron imaging system installed in the RADEN instrument was updated from previous studies.[39,42] For the current study, the PEFC was operated at currents of up to 1000 A and supplied with humidified gases, namely hydrogen/nitrogen at the anode (0.2–10 L min^{-1}) and air/nitrogen at the cathode (1.0/0.2–50/10 L min^{-1}), over a dew point range of 15–80 °C. Fig. 1a shows the cooling system used to perform the cold-start experiments (minimum start temperature of −30 °C), wherein this system consists of an in-house heat exchanger and a commercial chiller (FP89-HL, JULABO, Germany). Temperature-controlled Fluorinert (FC-3283, 3M Company, USA) with a high degree of neutron transmittance was circulated on both sides of the PEFC using a pump. The circulating system was used to regulate the cell temperature with minimal interference from the neutron beam, thereby allowing high-quality neutron images to be acquired. Silicone oil (10 L; KF-96-10cs, Shin-Etsu Chemical, Japan) was employed as the cooling medium in the chiller to cool the Fluorinert in the in-house heat exchanger. Rapid control of the cell temperature was achieved by switching from a cooling system (Fig. 1a) to a rapid heating system (Fig. 1b). Ethylene glycol (Nybrine Z-1, Nisso Shoji, Japan) was employed as the heating medium in the in-house heating circulator to secondarily heat Fluorinert through another in-house heat exchanger. A large amount of ethylene glycol was required to achieve a rapid temperature increase. The estimated heat capacity, which was mainly attributed to the aluminium pads (15 kg) and the Fluorinert component (7 kg), reached a total of 627 kJ K^{-1}, and the amount of heat required to raise the cell temperature from −30 to 0 °C in 1 min was estimated to be 8 kJ s^{-1}. To satisfy these requirements, a heat storage tank containing 20 L of ethylene glycol was prepared to achieve a maximum heating rate of 1.4 °C s^{-1} (using the heating medium at a temperature of 90 °C). In this study, the ethylene glycol temperature was set to 55 °C to achieve a heating rate of 0.5 °C s^{-1} to simulate the coolant temperature of a fuel cell stack during rapid cold starts.[35] Details of the switching system installed in the environmental chamber and the in-house rapid heating unit are provided in Fig. S1 and S2 (ESI†), respectively.

Fig. 1c shows an aluminium pad containing the circulating temperature-controlled Fluorinert. These pads are located on both sides of the automotive PEFC in a parallel-flow configuration upstream of the cathode. An engineered dome-shaped pad on the anode side was used to provide a uniform contact pressure distribution over the entire electrochemically active area, clamping only at the periphery (Fig. 1d). This improvement allowed water visualisation experiments to be performed over the entire electrochemically active area without the field-of-view limitations imposed by a cross-shaped fixture.[42]

The top panel of Fig. 1e shows the neutron transmission image of the automotive PEFC under dry conditions. Twelve thermocouples were inserted between the pad and the automotive PEFC at the cathode and anode, respectively, and a total of 24 points were measured simultaneously during neutron imaging. The water content in each pixel was determined from the difference in neutron transmittance between the dry and wet images using the Beer–Lambert law. The total water content was defined as the cumulative value of the electrochemically active area of the automotive PEFC. In addition, the water content was divided into four positions in the lateral direction to investigate the effect of the cathode gas flow position on the water content during the rapid cold starts (bottom panel of Fig. 1e). The positions upstream and downstream of the cathode correspond to positions 1 and 4, respectively. Because the segmentation area per position differed slightly upon insertion of the thermocouples, the water contents at positions 1–4 were expressed in terms of the water content per square centimetre. Fig. 1f illustrates a typical PEFC configuration consisting of CLs, GDLs and gas flow channels at the cathode and anode, which were separated using a PEM. The gases were supplied to the cathode and the anode in a counterflow

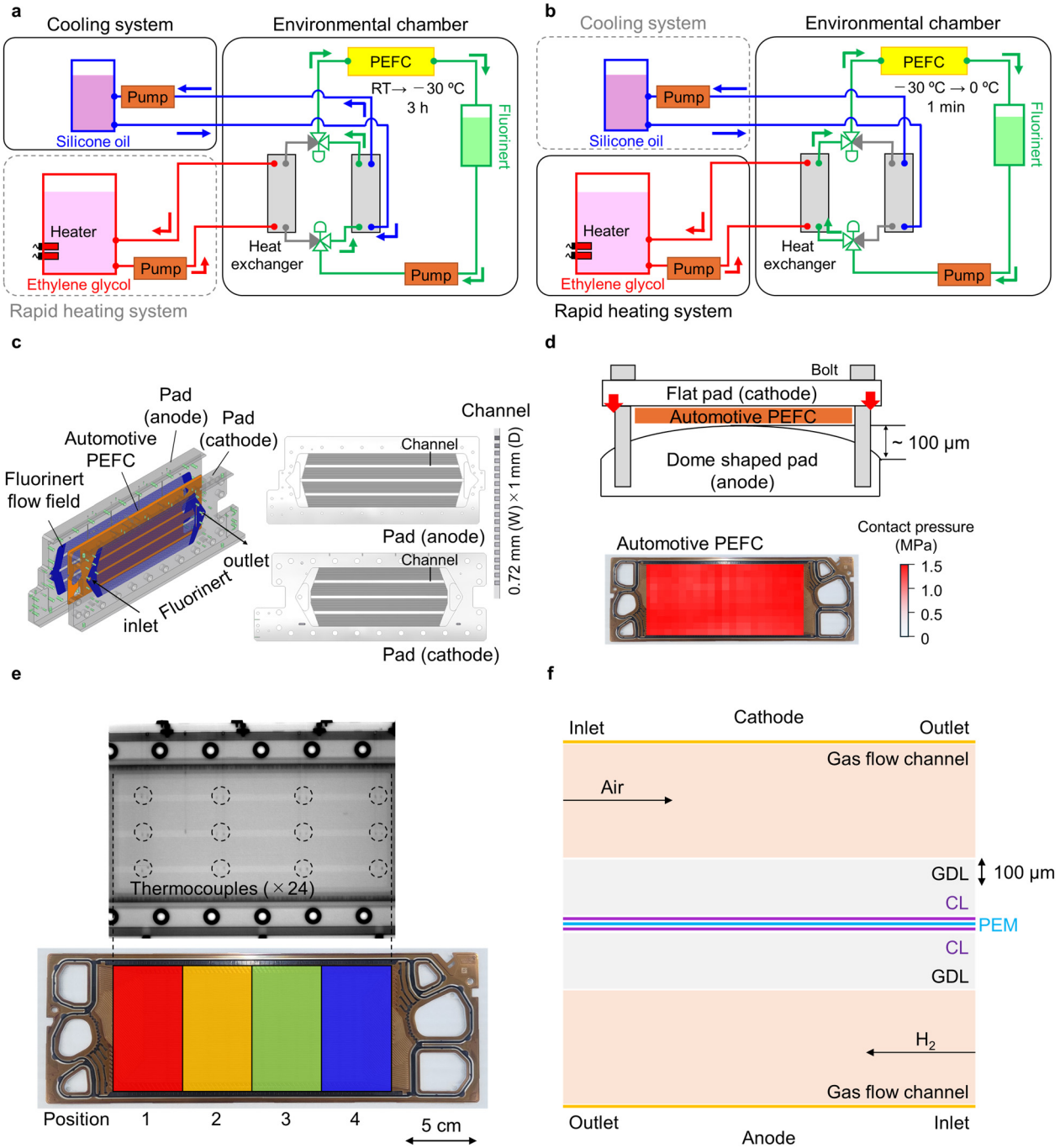

Fig. 1 Setup of the rapid cold start and automotive PEFC configuration. (a) Cooling and (b) rapid heating systems. (c) Pads circulating Fluorinert in a parallel-flow configuration upstream of the cathode. (d) Illustration of the dome-shaped pad and contact pressure distribution inside the automotive PEFC. (e) Neutron transmission image of a cell equipped with a single cell in a 2nd generation MIRAI (top) and photograph of the 2nd generation MIRAI (bottom). Positions 1–4 on the image show the segmentation areas employed for analysis. (f) Cross-sectional view of a typical laminated PEFC structure.

configuration through the gas flow channels in the flow-field plates.

Cold-start performance

Based on the consensus that the freezing point at the cathode depends on the cold-start temperature,[34] cold starts were studied at three different sub-zero temperatures. Fig. 2a shows the electrochemical performances during these cold starts, wherein it can be seen that the current maximum was observed immediately after the cold start. More specifically, at cold-start temperatures of −5.5 and −8.0 °C, a current maximum of 150 A was obtained, as defined by the air stoichiometry. In contrast, only 90% of the theoretical current (150 A) was achieved at a cold-start temperature of −12.0 °C. After reaching the current maximum, the current decreased rapidly at lower cold-start temperatures. The rapid heating mode was turned on 70 s after

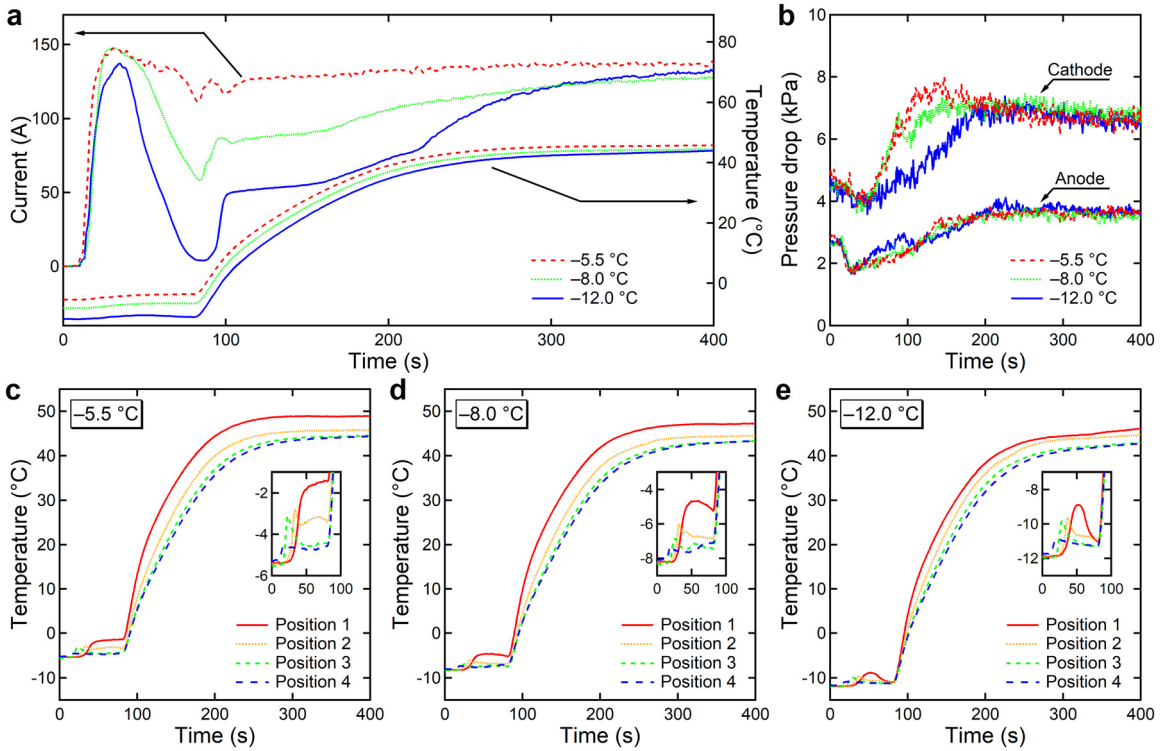

Fig. 2 Cold-start performances at three sub-zero temperatures. (a) Variation in the current with the average cell temperature. (b) Pressure drop from the cathode/anode inlet to the outlet over time at different temperatures. (c–e) In-plane temperature distributions at four vertically segmented positions.

the cold start to simulate the increase in coolant temperature in the fuel cell stack during an actual cold start.[35] At this point, the average cell temperature responded quickly, exceeding 0 °C in 10 s, with discontinuous jumps in the current. Even after reaching a typical operating temperature of 45 °C after 230 s of external heating, the current did not reach the expected maximum, and an additional time of ~100 s was required to recover to the current maximum. In addition, no significant performance degradation was observed during normal-temperature operation (45 °C), even after three repeated cold-start experiments (Fig. S3 of the ESI†). Notably, the cell temperature showed almost the same behaviour, despite the more pronounced delay in current recovery at lower cold-start temperatures. Freezing and thawing behaviour would be involved in the current recovery process. The mechanism based on *operando* neutron imaging data is discussed in the next subsection.

In addition, as shown in Fig. 2b, the pressure drops from the cathode/anode inlets to the outlet. The trend for the cathode was more variable than that for the anode, indicating that the cathode was more affected by the accumulation of produced water. For the cold-start processes performed between −5.5 and −8.0 °C, the pressure drop observed at the cathode increased during the current drop stage. This trend can be explained by considering ice formation in the cathode GDL and in the cathode gas flow channels. In contrast, the pressure drop was mitigated for the cold-start processes performed beyond −12.0 °C, suggesting that the adverse effect of ice formation on the cathode electrode was more severe in the CL than in the GDL and the gas flow channels. After reaching a steady state, the pressure drop remained essentially constant. The detection of Joule heating provides indirect evidence regarding the evolution of the power output during a cold start. Fig. 2c–e show the cell temperatures at four vertically segmented positions. It can be seen that immediately after the cold start, the cell temperature increased at the cathode outlet and gradually increased upstream (see insets, Fig. 2c–e). This result indicates that power generation started at the cathode outlet and shifted to the cathode inlet.

After the heating mode was turned on, the cell temperature increased downstream from the cathode inlet owing to the flow of the coolant (Fig. 1c). After reaching a steady state, the cell temperature at the cathode inlet was maintained at ~4 °C higher than that at the outlet. The temperature difference between the cathode inlet and outlet was Δ0.3 °C when the fuel cell was cooled to −12.0 °C. However, the cell temperature differences between the cathode and anode and between the top and bottom were only Δ0.1 °C (Fig. S4 of the ESI†).

Operando neutron imaging

Fig. 3 shows the neutron transmission images extracted from the time-lapse images (Videos S1–S3 of the ESI†) at three characteristic points, namely the current maximum at 30 s, the current drop at 80 s, and the current recovery at 150 s. The neutrons were attenuated by the accumulated liquid water, and the degree of attenuation (up to 5%) depended on the water content.

The maximum area-specific water contents, calculated from the porosity and thickness at the cathode CL and GDL, were below 1 and 20 mg cm^{-2}, respectively (see Fig. S3 and the ESI†

for details), corresponding to neutron attenuations of less than 0.5 and 8%, respectively (eqn (1)).

This trial calculation indicates that it is difficult to visually detect the water accumulation in the cathode CL from the difference in neutron transmittance, and it also suggests that the black shadows in Fig. 3 can be associated with water accumulation in the cathode GDL. The straight-line shadows reflect the geometry of the cathode gas flow channels, where water accumulated to a greater extent than at the cathode electrode (*i.e.*, the sum of the CL and GDL).[39,42]

In the neutron images recorded at the current maximum stage, a uniform water distribution was observed throughout the PEFC, with no water aggregates being detected in the cathode GDL or gas flow channels. These observations indicate that the produced water did not drain outside the cathode CL. In contrast, during the current drop stage, a non-uniform water accumulation was observed in the cathode GDL (and in the cathode gas flow channels at −5.5 °C) close to the cathode inlet. This non-uniform water distribution indicates that the power generation site was concentrated upstream of the cathode, as the amount of produced water corresponded to the current, suggesting that the produced water in the cathode CL was completely frozen downstream of the cathode. This trend is consistent with the cell-temperature distribution presented in Fig. 2c–e. During the current recovery stage, this non-uniform water accumulation was gradually mitigated (Fig. 3c, f and i; Videos S1–S3 of the ESI†). This result implies that the frozen water melted after reaching the freezing point. In addition, water aggregates were observed in the cathode outlet manifold (lower right segments in Fig. 3c and f).

Quantification of the water content

Fig. 4a–c show the temporal dependence of the area-specific water content at vertically segmented positions from upstream position 1 to downstream position 4 of the cathode. Quantitative analysis revealed that the water content near the cathode outlet increased immediately after the cold start. The water content at position 4 was ∼1 mg cm^{-2}, which corresponded to the allowable water content of the cathode CL. Thereafter, the water content near the cathode inlet exceeded that near the cathode outlet during the current drop stage. These results indicate that power generation started downstream of the cathode and gradually migrated upstream during the cold start, which is consistent with the temperature distribution results (Fig. 2c–e). During the current recovery stage, the amount of water near the cathode inlet decreased. This result indicates water migration downstream of the cathode due to ice thawing. Fig. 5 displays a schematic illustration of the water and ice locations at the cathode electrode during a rapid cold start based on pressure drop (Fig. 2b) and neutron imaging data (Fig. 4a–c).

As the cell temperature increased towards a normal operating temperature, the difference in the water content tended to decrease; however, even after the cell temperature reached a steady state, the water distribution still reflected the water distribution during the current recovery, which depended on the cold-start temperature. The difference between the water contents evaluated from the current and from the neutron transmittance (eqn (1) and (2)) provides insights into the discharged water content, *i.e.*, the drainage capacity.

Fig. 4d shows the temporal dependence of the total water content at the three different cold-start temperatures investigated here. At sub-zero temperatures, the water contents evaluated from the two datasets were in good agreement, indicating that most of the supercooled water generated during sub-zero power generation was stored within the cell, rather than being discharged. Water discharge outside the cell was observed after the total water content reached ∼800 mg at a cell temperature >0 °C.

In the steady state, the total water content was ∼1000 mg at all cold-start temperatures, suggesting that the drainage capacity after the cold start was identical at the three cold-start

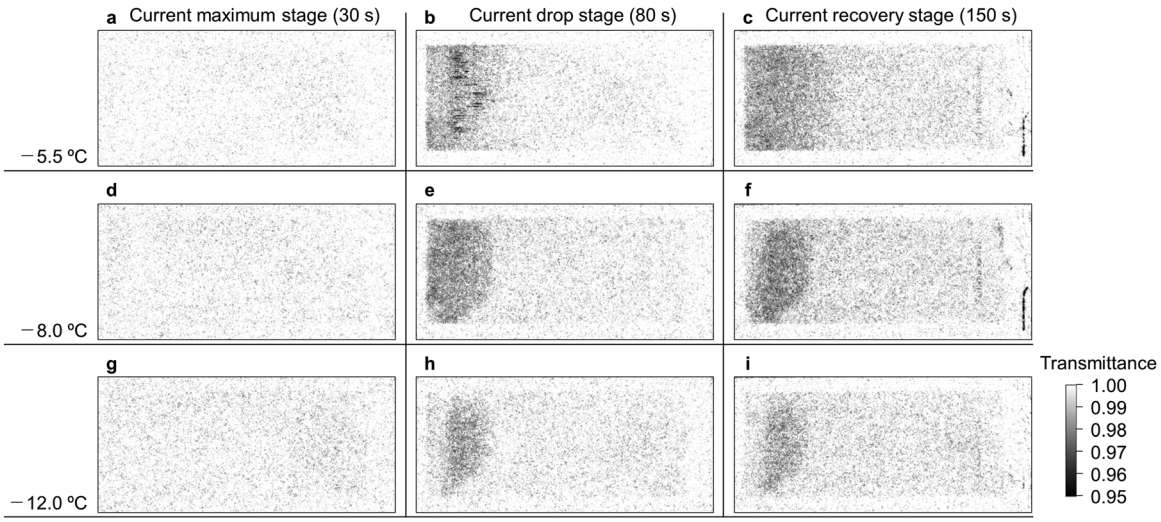

Fig. 3 Neutron transmission images during rapid cold starts. Images of (a–c) the current maximum, (d–f) the current drop and (g–i) the current recovery stages. (a, d and g) Images recorded at a cold-start temperature of −5.5 °C. (b, e and h) Images recorded at a cold-start temperature of −8.0 °C. (c, f and i) Images recorded at a cold start of −12.0 °C.

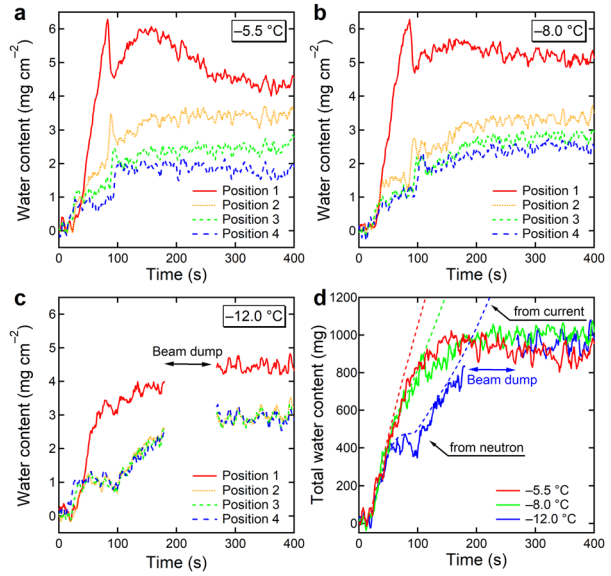

Fig. 4 Water content during rapid cold starts. In-plane water distribution at four vertically segmented positions for cold-start temperatures of (a) −5.5 °C, (b) −8.0 °C and (c) −12.0 °C. (d) Total water content evaluated from the neutron transmittance and current.

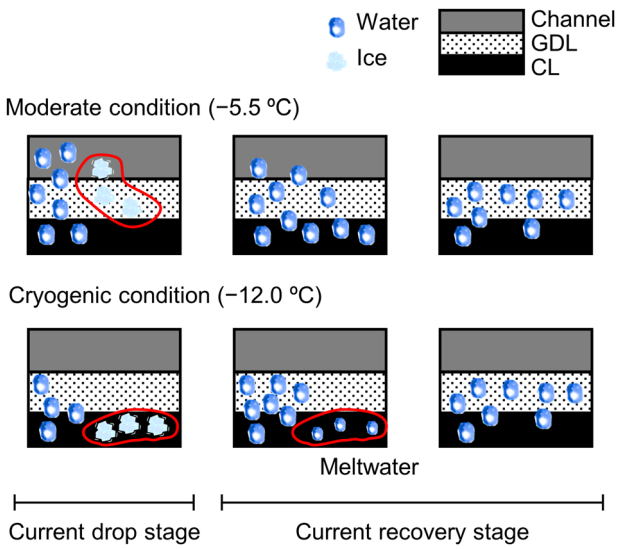

Fig. 5 Schematic illustration of the water and ice locations at the cathode electrode during rapid cold starts. The cathode electrode structure is not drawn to scale.

temperatures, regardless of the non-uniform water distribution (Fig. 4a–c). The allowable water contents calculated from the porosity and thickness at the cathode CL and GDL were ~150–200 and 4000–4500 mg, respectively (Fig. S5 of the ESI†), indicating that liquid water can accumulate at the cathode electrode up to a water saturation degree of ~0.2–0.25. This estimation agrees with previous studies based on the evaluation of small single cells using synchrotron X-ray radiography.[39,45]

Discussion

As shown in Fig. 3h, the cryogenic cold-start conditions resulted in ice formation in the cathode CL at sub-zero temperatures. This is consistent with the indirect evidence of a pressure drop (Fig. 2b) and previous *post-mortem* studies.[19–26] In contrast, ice aggregation in the GDL and cathode gas flow channels was confirmed under mild cold-start conditions (Fig. 3b). The supercooled water did not reach the cathode outlet at sub-zero temperatures, as evidenced by a comparison of the total water content in the cell with the produced water content (Fig. 4d). Importantly, the phase transition of metastable supercooled water to ice can be induced in multiple ways, such as through mechanical shock,[28] residual water[46] and migration to larger pores.[47–49] The initiated freezing process then extends over the entire cell, and freezing occurs within a short time. As previously reported, phase transitions associated with random ice nucleation have a high probability of freezing in large-sized PEFCs with a higher water content.[37] During a cold start in an automotive PEFC containing 500 mg of water (Fig. 4d), it is impossible for the supercooled water to travel several tens of centimetres and eventually discharge to the cathode outlet. These findings validate the conventional concept of how to break through a temperature of 0 °C before freezing of the produced water occurs during a cold start.

The observed water accumulation near the cathode inlet during the cold start (Fig. 3) indicates that concentration of the current occurred. This effect has also been observed in a fuel cell stack using current distribution analysis.[35] This can be explained by considering ice formation at the cathode outlet caused by the residual water after pre-conditioning,[35] as well as the produced water immediately after cold start. Under normal operating conditions, the produced water accumulates at the centre and downstream of the cathode rather than upstream.[39] The dry air supplied during the purging process in the pre-conditioning step prioritises water evaporation at the cathode inlet,[35,50] and so a long purge protocol causes the PEM to over-dry and lose the proton conductivity required for power generation. This trade-off effect masks the elimination of residual water near the cathode outlet. A small amount of residual water (several tens of milligrams for the entire automotive PEFC) was present in the hard-to-evaporate CL (Fig. 4a–c), suggesting the need to consider other approaches, such as coolant heating,[51] gas heating,[52] electric heating[53] and hydrogen pump heating,[54] as well as optimisation of the purge protocols.

Importantly, in the current study, in-plane water distribution was visualised for the first time during the rapid heating of an automotive PEFC from sub-zero temperatures. This new observation sheds light on the slow current recovery behaviour after a successful cold start. The current recovery process is related to the improvement in the cold-start efficiency and shorter cold-start times.

Several previous studies have reported slow current recovery behaviours in fuel cell stacks.[17,18,35] For example, Tabe *et al.*[23] claimed that the meltwater after a cold start, which is different from the produced water distribution during normal-temperature operation, blocks the oxygen supply to the cathode

CL, resulting in a deterioration of the electrochemical performance. Due to the detection limit of neutron imaging (see the Experimental section), there is no direct evidence of an adsorbed nano-scale water layer that inhibits oxygen molecules from accessing the platinum surface.

However, the inhomogeneous in-plane water distribution during the cold start was detected, even after reaching normal operating conditions (Fig. 3). In addition, the non-uniformity was more pronounced at lower cold-start temperatures (Fig. 4a–c). Freezing propagation would promote water accumulation in micro-scale regions where water is difficult to evaporate (*e.g.*, cathode GDL/CL interfaces and cathode CL pores). Moreover, lower cold-start temperatures increased the probability of freezing in the cathode CL, which contributed to the subsequent non-uniformity in the water distribution. Switching to a mode that operates the fuel cell stack at high temperatures effectively accelerates water evaporation in the cathode CL, thereby erasing the water distribution history after a rapid cold start.

Experimental

Operando neutron imaging system

A 20 μm-thick 2nd generation MIRAI catalyst-coated membrane (CCM) was employed for the purpose of this study. The CCM contained an 8.5 μm-thick reinforced PEM,[39] in which some of the proton sites were replaced by Ce ions for radical quenching. The anode CL contained a Pt catalyst (0.03 mg_{Pt} cm^{-2}) supported on carbon black, while the cathode CL contained a Pt–Co alloy catalyst (0.17 mg_{Pt} cm^{-2}) supported on mesoporous carbon nanodendrites.[55] An ionomer with a three-times higher oxygen permeability than conventional Nafion ionomers was used in the cathode CL.[56] The membrane electrode assembly was prepared by sandwiching GDLs with microporous layers on both sides of the CCM. A partially narrowed flow-field plate was used at the cathode to compress and assemble the membrane electrode assembly.[43] The contact pressure was measured using a pressure measurement film (Prescale LLW, Fujifilm, Japan).

Cold-start procedure

The automotive PEFC was powered by a gas control unit (custom order, Enoah, Japan), a chiller (RKS1503J, ORION Machinery, Japan) and an electronic load unit (KFM2150 SYSTEM, PLZ1004WS and PLZ2004WB × 2, KIKUSUI, Japan). The cold-start tests at three different sub-zero temperatures were sequentially performed from lower cold-start temperatures using the same cell. The cold-start procedure consisted of four steps, namely pre-conditioning, external cooling, cold-start and external heating. Pre-conditioning, which included drying, wetting and purging, was performed to overwrite the history of the water accumulated during the previous power generation process. The numerical parameters for the pre-conditioning stage can be found in the literature.[35] After pre-conditioning, the gas supply was stopped, and cooling was conducted until reaching the desired cold-start temperature; this temperature was achieved by controlling the coolant temperature. After stabilisation of the cell temperature, a rapid cold start was performed in the constant-voltage mode (0.2 V, 1.4 L min^{-1} dry hydrogen flow at the anode, 2.6 L min^{-1} dry air flow at the cathode). The programme start was defined as the start time (0 s). The cell voltage was then swept to reach 0.2 V after 20 s. Subsequently, the external heating unit was switched on for 70 s.

Neutron imaging

Operando neutron radiography was performed at the RADEN instrument in J-PARC. An automotive PEFC equipped with an environmental chamber was installed on the sample stage 23 m from the neutron source. A neutron detector was placed immediately behind the PEFC. The neutron beam was collimated using a 50.1 mm-diameter aperture installed in the shutter section. The neutron wavelength range was set to 0.23–0.88 nm using a wavelength-definition chopper system.[38] The beam divergence L/D was 398, where D is the aperture width and L is the distance from the aperture to the detector. The detector system consisted of a CMOS camera (ORCA Flash4.0, Hamamatsu Photonics K.K., Japan), an optical image intensifier (C14245-12112-A1, Hamamatsu Photonics K.K.), an optical lens (Nikkor 35 mm, Nikon, Japan) and a 0.3 mm-thick ZnO/^{6}LiF scintillator screen (NDFast, Scintacor, UK). Sequential image capture was performed with a 1 s exposure. The proton-beam power used in the measurements was 770 kW. The raw data were corrected with a dark current image and then compensated for incident beam intensity fluctuations and detector damage due to the high-intensity neutron irradiation.[42] This image processing was performed using ImageJ software.[57]

Quantification of the water content

The water coent was evaluated using neutron transmission imaging and power generation. The water content obtained from the neutron transmittance ($m_{neutron}$) was calculated using the Beer–Lambert law:

$$m_{\mathrm{neutron}} = \frac{Ad}{\mu}\ln\left(\frac{T_{\mathrm{dry}}}{T_{\mathrm{wet}}}\right) \quad (1)$$

where d is the density of water, A is an arbitrary analysis area, μ is the conversion coefficient for H_2O, T_{dry} is the neutron transmittance intensity at the open-circuit voltage under a dry gas flow and T_{wet} is the neutron transmittance intensity during power generation. In this study, d was set to 1.0 mg cm^{-3} and was considered a temperature-independent constant. A water-filled quartz cell was used to evaluate μ, and a calibration value of 0.0042 cm^{-1} was obtained. The detection limit depends on the intensity fluctuations of incident neutron beams and the shot noise inherent in the neutron detector. The quantitative reliability was ±0.5 mg cm^{-2} of the water content (±5 μm in water thickness), as shown in Fig. S6 of the ESI.†

The water content obtained from the electrochemical measurements ($m_{current}$) was calculated using Faraday's law:

$$m_{\mathrm{current}} = \frac{M}{2F}\int I\,\mathrm{d}t \quad (2)$$

where M is the molar weight of H_2O, I is the current and F is Faraday's constant.

Conclusions

An *operando* neutron imaging system was effectively established to evaluate cold-start tests in automotive PEFCs, with the aim of bridging the gap between small cell tests for liquid/ice visualisation and fuel cell stack tests that were previously inaccessible for visualisation studies. The present study demonstrated for the first time that the cold-start performance of a fuel cell stack could be successfully reproduced in an automotive single cell while simultaneously measuring the water distribution using neutron radiography. This observation justifies the cold-start strategies for fuel cell stacks proposed by previous small cell studies.[12–15,19–26,28–32] Additionally, neutron imaging highlighted the effects of residual water and meltwater on the cold-start performance. The observed cell voltage drop, which was recovered upon refreshing the cell with a gas purge, was considered analogous to the memory effect in batteries.[58,59] This finding offers inspiration for improving the cold-start performances of fuel cell stacks and will be expected to benefit the fuel cell community.

Author contributions

Y. H. designed the experiments and analysed the neutron imaging data. S. H. designed the experimental setup for neutron imaging experiments. W. Y., Y. H., S. H., F. S., Y. M., H. H., H. N., T. K. and S. K. performed the neutron imaging experiments. W. Y. interpreted the experimental results and prepared the manuscript. S. K. supervised the project. All authors contributed to the revision of the original manuscript and approved the final version.

Data availability

The data that support the findings of this study are available in the paper and the ESI.† Data are available upon reasonable request from the corresponding author.

Conflicts of interest

The automotive PEFC, identified as a second-generation MIRAI used for the measurements, was provided by Toyota Motor Corporation. Such identification does not imply recommendations or endorsements by Toyota Central R&D Labs., Inc. or Toyota Motor Corporation. All disclosed information regarding the commercial product is provided in the manuscript.

Acknowledgements

The authors thank Mr Tadao Ozawa, Mr Naoki Katayama, Dr Tadanobu Ueda and Ms Miwa Kanazawa (Toyota Central R&D Labs., Inc.) for designing and fabricating the in-house rapid heating circulator. Neutron imaging was conducted at BL22 with the approval of J-PARC (proposal no. 2019L0403 and 2021B0317).

References

1 K. Jiao, J. Xuan, Q. Du, Z. Bao, B. Xie, B. Wang, Y. Zhao, L. Fan, H. Wang, Z. Hou, S. Huo, N. P. Brandon, Y. Yin and M. D. Guiver, *Nature*, 2021, **95**, 361–369.
2 D. A. Cullen, K. C. Neyerlin, R. K. Ahluwalia, R. Mukundan, K. L. More, R. L. Borup, A. Z. Weber, D. J. Myers and A. Kusoglu, *Nat. Energy*, 2021, **6**, 462–474.
3 G. A. Lindquist, Q. Xu, S. Z. Oener and S. W. Boettcher, *Joule*, 2020, **4**, 2549–2561.
4 M. F. Lagadec and A. Grimaud, *Nat. Mater.*, 2020, **19**, 1140–1150.
5 R. Iwata, L. Zhang, K. L. Wilke, S. Gong, M. He, B. M. Gallant and E. N. Wang, *Joule*, 2021, **5**, 887–900.
6 N. Kato, S. Mizuno, M. Shiozawa, N. Nojiri, Y. Kawai, K. Fukumoto, T. Morikawa and Y. Takeda, *Joule*, 2021, **5**, 687–705.
7 T. Morikawa, S. Sato, K. Sekizawa, T. M. Suzuki and T. Arai, *Acc. Chem. Res.*, 2022, **55**, 933–943.
8 H. Nishiyama, T. Yamada, M. Nakabayashi, Y. Maehara, M. Yamaguchi, Y. Kuromiya, Y. Nagatsuma, H. Tokudome, S. Akiyama, T. Watanabe, R. Narushima, S. Okunaka, N. Shibata, T. Takata, T. Hisatomi and K. Domen, *Nature*, 2021, **598**, 304–307.
9 J. Liang, L. Fan, Q. Du, Y. Yin and K. Jiao, *Adv. Sci.*, 2023, **10**, 2302151.
10 K. Kodama, T. Nagai, A. Kuwaki, R. Jinnouchi and Y. Morimoto, *Nat. Nanotechnol.*, 2021, **16**, 140–147.
11 K. Sekizawa, N. Kitamura, K. Manabe, Y. Nonobe, M. Kizaki and K. Kojima, *ECS Trans.*, 2010, **33**, 1947–1957.
12 Y. Ishikawa, T. Morita, K. Nakata, K. Yoshida and M. Shiozawa, *J. Power Sources*, 2007, **163**, 708–712.
13 Y. Ishikawa, H. Hamada, M. Uehara and M. Shiozawa, *J. Power Sources*, 2008, **179**, 547–552.
14 J. Mishler, Y. Wang, R. Lujan, R. Mukundan and R. L. Borup, *J. Electrochem. Soc.*, 2013, **160**, F514–F521.
15 A. Pistono and C. A. Rice, *J. Electrochem. Soc.*, 2017, **164**, F582–590.
16 A. A. Amamou, S. Kelouwani, L. Boulon and K. Agbossou, *IEEE Access*, 2016, **4**, 4989–5002.
17 J. St-Pierre, J. Roberts, K. Colbow, S. Campbell and A. Nelson, *J. New Mater. Electrochem. Syst.*, 2005, **8**, 163–176.
18 K. Hu, T. Chu, F. Li, B. Wang, Z. Zhang and T. Liu, *Int. J. Hydrogen Energy*, 2021, **46**, 31788–31797.
19 S. Kim and M. M. Mench, *J. Power Sources*, 2007, **174**, 206–220.
20 S. Kim, B. K. Ahn and M. M. Mench, *J. Power Sources*, 2008, **179**, 140–146.
21 E. L. Thompson, J. Jorne, W. Gu and H. A. Gasteiger, *J. Electrochem. Soc.*, 2008, **155**, B625–B634.
22 E. L. Thompson, J. Jorne, W. Gu and H. A. Gasteiger, *J. Electrochem. Soc.*, 2008, **155**, B887–B896.
23 Y. Tabe, M. Saito, K. Fukui and T. Chikahisa, *J. Power Sources*, 2012, **208**, 366–373.

24 Y. Tabe, K. Yamada, R. Ichikawa, Y. Aoyama, K. Suzuki and T. Chikahisa, *J. Electrochem. Soc.*, 2016, **163**, F1139–F1145.
25 Y. Tabe, N. Wakatake, Y. Ishima and T. Chikahisa, *J. Electrochem. Soc.*, 2021, **168**, 064502.
26 J. Mishler, Y. Wang, P. P. Mukherjee, R. Mukundan and R. L. Borup, *Electrochim. Acta*, 2012, **65**, 127–133.
27 M. Khandelwal and M. M. Mench, *J. Power Sources*, 2010, **195**, 6549–6558.
28 P. Oberholzer, P. Boillat, R. Siegrist, R. Perego, A. Kästner, E. Lehmann, G. G. Scherer and A. Wokauna, *J. Electrochem. Soc.*, 2012, **159**, B235–B245.
29 A. Santamaria, H.-Y. Tang, J. W. Park, G.-G. Park and Y.-J. Sohn, *Int. J. Hydrogen Energy*, 2012, **37**, 10836–10843.
30 N. Macauley, R. W. Lujan, D. Spernjak, D. S. Hussey, D. L. Jacobson, K. More, R. L. Borup and R. Mukundana, *J. Electrochem. Soc.*, 2016, **163**, F1317–F1329.
31 P. Stahl, J. Biesdorf, P. Boillat and K. A. Friedrich, *J. Electrochem. Soc.*, 2016, **163**, F1535–F1542.
32 M. Sabharwal, F. N. Büchi, S. Nagashima, F. Marone and J. Eller, *J. Power Sources*, 2021, **489**, 229447.
33 K. Jiao, I. E. Alaefour, G. Karimi and X. Li, *Int. J. Hydrogen Energy*, 2011, **36**, 11832–11845.
34 C. A. Rice, *J. Electrochem. Soc.*, 2021, **168**, 044513.
35 T. Takahashi, Y. Kokubo, K. Murata, O. Hotaka, S. Hasegawa, Y. Tachikawa, M. Nishihara, J. Matsuda, T. Kitahara, S. M. Lyth, A. Hayashi and K. Sasaki, *Int. J. Hydrogen Energy*, 2022, **47**, 41111–41123.
36 M. Khandelwal, S. Lee and M. M. Mench, *J. Power Sources*, 2007, **172**, 816–830.
37 J. Biesdorf, P. Stahl, M. Siegwart, T. J. Schmidt and P. Boillat, *J. Electrochem. Soc.*, 2015, **162**, F1231–F1235.
38 T. Shinohara, T. Kai, K. Oikawa, T. Nakatani, M. Segawa, K. Hiroi, Y. Su, M. Ooi, M. Harada, H. Iikura, H. Hayashida, J. D. Parker, Y. Matsumoto, T. Kamiyama, H. Sato and Y. Kiyanagi, *Rev. Sci. Instrum.*, 2020, **91**, 043302.
39 W. Yoshimune, Y. Higuchi, A. Kato, S. Hibi, S. Yamaguchi, Y. Matsumoto, H. Hayashida, H. Nozaki, T. Shinohara and S. Kato, *ACS Energy Lett.*, 2023, **8**, 3485–3487.
40 Y. Higuchi, D. Setoyama, K. Isegawa, Y. Tsuchikawa, Y. Matsumoto, J. D. Parker, T. Shinohara and Y. Nagai, *Phys. Chem. Chem. Phys.*, 2021, **23**, 1062–1071.
41 K. Isegawa, D. Setoyama, Y. Higuchi, Y. Matsumoto, Y. Nagai and T. Shinohara, *Nucl. Instrum. Methods Phys. Res., Sect. A*, 2022, **1040**, 167260.
42 Y. Higuchi, W. Yoshimune, S. Kato, S. Hibi, D. Setoyama, K. Isegawa, Y. Matsumoto, H. Hayashida, H. Nozaki, M. Harada, N. Fukaya, T. Suzuki, T. Shinohara and Y. Nagai, *Commun. Eng.*, 2024, **3**, 33.
43 T. Yoshizumi, H. Kubo and M. Okumura, Development of High-Performance FC Stack for the New MIRAI, SAE Technical Paper 2021-01-0740, 2021, DOI: **10.4271/2021-01-0740**.
44 T. Takahashi, T. Ikeda, K. Murata, O. Hotaka, S. Hasegawa, Y. Tachikawa, M. Nishihara, J. Matsuda, T. Kitahara, S. M. Lyth, A. Hayashi and K. Sasaki, *J. Electrochem. Soc.*, 2022, **169**, 044523.
45 W. Yoshimune, A. Kato, T. Hayakawa, S. Yamaguchi and S. Kato, *Adv. Energy Sustainability Res.*, 2024, **5** 2400126.
46 P. Stahl, J. Biesdorf, P. Boillat and K. A. Friedrich, *Fuel Cells*, 2017, **17**, 778–785.
47 Y. Ishikawa, M. Shiozawa, M. Kondo and K. Ito, *Int. J. Heat Mass Transfer*, 2014, **74**, 215–227.
48 S. Wang, Y. Sun, F. Huang and J. Zhang, *J. Electrochem. Soc.*, 2019, **166**, F860–F864.
49 K. Wang, S. Wang and Y. Zhu, *J. Power Sources*, 2024, **602**, 234310.
50 R. Lin, X. Lin, Y. Weng and Y. Ren, *Int. J. Hydrogen Energy*, 2015, **40**, 7370–7381.
51 G. Montaner Ríos, J. Schirmer, C. Gentner and J. Kallo, *Appl. Energy*, 2020, **279**, 115813.
52 Z. Zhan, C. Yuan, Z. Hu, H. Wang, P. C. Sui, N. Djilali and M. Pan, *Energy*, 2018, **162**, 1029–1040.
53 L. Li, S. Wang, L. Yue and G. Wang, *Appl. Energy*, 2019, **254**, 113716.
54 H. Xu, S. Wang and J. Zhang, *J. Electrochem. Soc.*, 2023, **170**, 024511.
55 V. Yarlagadda, M. K. Carpenter, T. E. Moylan, R. S. Kukreja, R. Koestner, W. Gu, L. Thompson and A. Kongkanand, *ACS Energy Lett.*, 2018, **3**, 618–621.
56 R. Jinnouchi, K. Kudo, K. Kodama, N. Kitano, T. Suzuki, S. Minami, K. Shinozaki, N. Hasegawa and A. Shinohara, *Nat. Commun.*, 2021, **12**, 4956.
57 C. A. Schneider, W. S. Rasband and K. W. Eliceiri, *Nat. Methods*, 2012, **9**, 671–675.
58 T. Sasaki, Y. Ukyo and P. Novák, *Nat. Mater.*, 2013, **12**, 569–575.
59 F. Roeder and S. Ramasubramanian, *Energy Technol.*, 2022, **10**, 2200627.

